AGU PUBLICATIONS

JGR

Journal of Geophysical Research: Earth Surface

RESEARCH ARTICLE
10.1002/2015JF003667

Modeling ice dynamic contributions to sea level rise from the Antarctic Peninsula

C. Schannwell[1,2], N. E. Barrand[1], and V. Radić[3]

[1]School of Geography, Earth and Environmental Sciences, University of Birmingham, Birmingham, UK, [2]British Antarctic Survey, Natural Environment Research Council, Cambridge, UK, [3]Department of Earth, Ocean and Atmospheric Sciences, University of British Columbia, Vancouver, British Columbia, Canada

Key Points:
- Ice shelf collapse timing is estimated using GCM temperature fields
- Grounding line retreat is estimated using a new statistical parameterization
- This provides scenario-based ice dynamical sea level rise projections

Correspondence to:
C. Schannwell,
cxs400@bham.ac.uk

Citation:
Schannwell, C., N. E. Barrand, and V. Radić (2015), Modeling ice dynamic contributions to sea level rise from the Antarctic Peninsula, *J. Geophys. Res. Earth Surf.*, *120*, 2374–2392, doi:10.1002/2015JF003667.

Received 9 JUL 2015
Accepted 3 NOV 2015
Accepted article online 6 NOV 2015
Published online 30 NOV 2015

Abstract The future ice dynamical contribution to sea level rise (SLR) from 199 ice shelf nourishing drainage basins of the Antarctic Peninsula Ice Sheet is simulated, using the British Antarctic Survey Antarctic Peninsula Ice Sheet Model. Simulations of the grounded ice sheet include response to ice shelf collapse, estimated by tracking thermal ice shelf viability limits in 14 Intergovernmental Panel on Climate Change global climate models ensemble temperature projections. Grounding line retreat in response to ice shelf collapse is parameterized with a new multivariate linear regression model utilizing a range of glaciological and geometric predictor variables. Multimodel means project SLR up to 9.4 mm sea level equivalent (SLE) by 2200, and up to 19 mm SLE by 2300. Rates of SLR from individual drainage basins throughout the peninsula are similar to 2100, yet diverge between 2100 and 2300 due to individual basin characteristics. Major contributors to SLR are the outlet glaciers feeding southern George VI Ice Shelf, accounting for >75% of total SLR in some model runs. Ice sheet thinning induced by ice-shelf removal is large (up to ~500 m), especially in Palmer Land in the southern Antarctic Peninsula, and may propagate as far as 135 km inland. These results emphasize the importance of the ice dynamical contribution to future sea level of the APIS on decadal to centennial timescales.

1. Introduction

Over the last century, the Antarctic Peninsula (AP) region has warmed by 3.7±1.6°C [*Vaughan et al.*, 2003]. This warming has been accompanied by a variety of responses, such as receding glacier fronts [*Cook et al.*, 2005], rising ocean temperatures [*Meredith and King*, 2005], prolonged melt season duration [*Vaughan*, 2006; *Barrand et al.*, 2013a; *Luckman et al.*, 2014], increased snowfall [*Turner et al.*, 2013], and retreat and disintegration of major fringing ice shelves [e.g., *Rott et al.*, 1996; *Scambos et al.*, 2000; *Cook and Vaughan*, 2010]. This removal of ice shelves has led to speed up [e.g., *De Angelis and Skvarca*, 2003; *Rott et al.*, 2011] and subsequent dynamic thinning of outlet glaciers [e.g., *Rignot et al.*, 2004; *Pritchard et al.*, 2009], contributing to sea level rise (SLR). Up until 2009, SLR contributions from the Antarctic Peninsula Ice Sheet (APIS) (~0.07 mm a^{-1}) and its surrounding islands were similar in magnitude to regional land-ice contributions from Alaska and the Canadian Arctic [*Hock et al.*, 2009; *Jacob et al.*, 2012; *Sasgen et al.*, 2013; *McMillan et al.*, 2014]. However, recent studies suggest that mass loss in the southern APIS has accelerated dramatically since 2010, contributing ~0.15 mm a^{-1} to overall SLR [*Wouters et al.*, 2015]. This recent dramatic increase in mass loss has been attributed to ice dynamical processes. Efforts to project SLR from this region have been mostly restricted to glaciers and ice caps of Antarctic and sub-Antarctic islands and were exclusively based on modeling the surface mass balance without consideration of glacier flow and iceberg calving [e.g., *Radic and Hock*, 2011; *Radic et al.*, 2014]. Using temperature and precipitation scenarios from an ensemble of global climate models (GCMs), these projections suggest that the surface mass loss of glaciers and ice caps on Antarctic and sub-Antarctic islands will continue over the next 100 years and could contribute between 5 and 40 mm SLE by the end of the 21st century [*Radic and Hock*, 2011; *Radic et al.*, 2014]. However, these projections do not include ice dynamic contributions to SLR from APIS following future ice shelf collapse and therefore will most likely underestimate the actual SLR contribution from the AP region.

Given the short response times of outlet glaciers in the AP [*Barrand et al.*, 2013b], ice dynamic SLR contributions resulting from continuing and future ice shelf retreats will exceed those from surface mass loss on decadal timescales [e.g., *Rignot et al.*, 2005]. *Scambos et al.* [2014] estimated the SLR contribution from glacier speedup, inland thinning, and retreat of the grounding line (point where glacier ice becomes afloat)

following the collapse of Larsen B Ice Shelf at 0.03 mm a^{-1}. It is expected that this contribution will diminish over time until outlet glaciers have adjusted to the new boundary conditions [*Schoof*, 2007]. The timescale for adjustment back to steady state conditions following ice shelf collapse is unknown, but presently outlet glaciers formerly feeding into Larsen A Ice Shelf are still thinning, ~20 years after ice shelf collapse, albeit at a decreasing rate [*Rott et al.*, 2014].

Modeling ice dynamic SLR following ice shelf breakup requires knowledge of the following: (i) the initial position of the grounding line, (ii) the timing of ice shelf collapse, and (iii) migration of the grounding line following ice shelf breakup.

Locating the position of the grounding line is not straightforward as the grounding line may be a gradual transition from grounded to floating ice conditions [*Corr et al.*, 2001; *Brunt et al.*, 2010]. The length of this transitional zone is typically in the order of a few kilometers across the grounding line [*Brunt et al.*, 2010]. Owing to the scale and inaccessibility of the grounding zone, remote sensing techniques are commonly used to map the position of the grounding line. In general, two differing types of remote sensing techniques are used: dynamic mapping using differential satellite radar interferometry (DInSAR) [e.g., *Brunt et al.*, 2010; *Rignot et al.*, 2011] or "static" mapping using Visible and Near-Infrared (VNIR) band satellite imagery [e.g., *Scambos et al.*, 2007; *Fricker et al.*, 2009]. However, each method maps a different point in the transitional zone. Dynamic mapping approximates the landward limit of the ice flexure zone as the position of the grounding line, whereas static mapping approximates the break in surface slope as the position of the grounding line [*Brunt et al.*, 2010]. In the absence of in situ grounding line positions [*Horgan and Anandakrishnan*, 2006; *Pattyn et al.*, 2013], intercomparison of remote sensing techniques suggests that positions can deviate by ~10 km in Antarctica, with higher deviations possible in lightly grounded areas [*Fricker et al.*, 2009; *Rignot et al.*, 2011]. The best agreement is reached in areas of slow moving ice, steep slopes, and relatively simple surface topography [*Fricker et al.*, 2009; *Rignot et al.*, 2011].

The position of the grounding line is expected to change in response to ice shelf collapse [e.g., *Rott et al.*, 2002; *Rignot et al.*, 2004; *Schoof*, 2007]. Therefore, knowledge of the timing of future ice shelf collapse and understanding the processes governing ice shelf instability are vital. Most of the abrupt ice shelf breakup events in the past have been linked to a warming climate [*Cook and Vaughan*, 2010]. In addition, satellite observations have shown that Antarctic ice shelves have experienced increased melting at their base [e.g., *Shepherd et al.*, 2003, 2010; *Rignot et al.*, 2013]. Under larger ice shelves, cold and dense high-salinity shelf water intrudes into the ice shelf cavity. Due to the increased pressure with depth, the freezing temperature of seawater is lowered. This leaves the high-salinity shelf water with heat available to melt the base of the ice shelf, releasing cold and fresh meltwater at depth. As this meltwater rises, the increasing temperature results in the meltwater becoming supercooled and freezing onto the base of the shelf. In contrast, smaller ice shelves are directly influenced by Circumpolar Deep Water (CDW) upwelling from the deep ocean [*Holland et al.*, 2008]. CDW is a relatively warm (over 1°C) and dense deep water mass with the potential to cause high melt rates at the bottom of ice shelves [*Rignot and Jacobs*, 2002; *Holland et al.*, 2008]. Typically, CDW intrudes into the ice shelf cavity along bathymetric troughs, driving melt at the underside of the ice shelf. Many major outlet glaciers are located at the head of these eroded troughs and are therefore susceptible to CDW intrusions [*Pritchard et al.*, 2012]. However, it is still poorly understood what controls these CDW intrusions.

In the AP region some fringing ice shelves might be vulnerable to CDW intrusions, e.g., George VI Ice Shelf [e.g., *Jenkins and Jacobs*, 2008], but the scarcity of in situ oceanographic data makes testing this hypothesis difficult. The most recent retreat and collapse of Larsen B Ice Shelf has been attributed to increased surface ponding and enhanced surface crevasse fracture [*Scambos et al.*, 2000; *van den Broeke*, 2005]. However, prior to final disintegration, Larsen B Ice Shelf had experienced a period of increased thinning, leaving the ice shelf vulnerable to hydrofracturing. *Shepherd et al.* [2003] suggested that this increased thinning was ocean-induced, warmer ocean water leading to higher basal melt rates. Other studies have suggested that at least part of the observed ice shelf thinning could be attributed to firn-air compaction [e.g., *Holland et al.*, 2011; *Kuipers Munneke et al.*, 2014]. *Holland et al.* [2015] estimate that basal melting (and/or ice flux divergence) and firn-air compaction contribute about equally to the present-day surface lowering of Larsen C Ice Shelf. They argue that for this particular ice shelf, at least two different forcings play a vital role in ice shelf instability with other factors such as the stress field and marine ice most likely also influencing the ice shelf's stability [*Kulessa et al.*, 2014; *Jansen et al.*, 2015].

Due to the complexity of the governing processes leading to ice shelf instability, data-led proxy approaches have previously been used to estimate the timing of ice shelf collapse [e.g., *Vaughan and Doake*, 1996; *Fyke et al.*, 2010]. Most commonly accepted is the approach that the geographical distribution of ice shelves in the AP region follows a climatic viability limit. The concept of a thermal limit of viability for ice shelves was first introduced by *Mercer* [1978] who observed that the geographical extent of ice shelves around the AP follows the 0°C isotherm of the warmest month of the year. As the density of available surface air temperature data improved, this thermal viability limit was slightly adjusted. *Vaughan and Doake* [1996] suggested the −5°C mean annual 2 m air temperature isotherm as the thermal viability limit. *Morris and Vaughan* [2003] then further refined the thermal viability limit based on observations that showed stable configurations for ice shelves south of the −9°C isotherm, no ice shelves present north of the −5°C isotherm, and ice shelves situated between these isotherms showing progressive retreat.

To provide more realistic SLR projections from ice dynamic adjustment following ice shelf collapse, ice sheet models need to account for the expected migration of the grounding line [e.g., *Pattyn et al.*, 2013]. This problem can be tackled twofold; either by modeling the complete system of grounded and floating ice sheet and tracking the grounding line over time or by modeling the grounded ice only and parameterizing the expected grounding line migration. Modeling ice sheet dynamics in full requires calculations of the 3-dimensional equation of fluid flow (Stokes equations). To reduce complexity and permit more computationally efficient ice sheet models, ice flow approximations are commonly used [e.g., *Hindmarsh*, 2004; *Pattyn et al.*, 2013]. Ice flow in the grounded ice sheet is dominated by vertical shear and controlled by basal drag (except for ice streams), whereas in the floating ice sheet, ice flow is dominated by longitudinal stretching and experiences negligible amount of basal traction [e.g., *Schoof*, 2007; *Pollard and DeConto*, 2012]. Several ice flow approximations are available for the two different flow regimes, representing various levels of sophistication. If ice flow approximations are used in the ice sheet model, both ice flow regimes require mechanical coupling to allow explicit grounding line migration modeling [e.g., *Goldberg et al.*, 2009; *Pattyn et al.*, 2013]. Even then the migration rate of the grounding line and its positional accuracy vary greatly across ice sheet models. These discrepancies reflect differences in the sophistication of the mechanical ice flow model, the numerical implementation of the ice sheet model, and the grid resolution [e.g., *Vieli and Payne*, 2005; *Cornford et al.*, 2013]. The level of complexity can be greatly reduced by only modeling the grounded ice sheet with the most commonly used shallow ice approximation (SIA) [*Hutter*, 1983]. The challenge of having to mechanically couple two different ice flow regimes vanishes but since the SIA is not valid at ice divides and grounding lines, it automatically excludes explicit modeling of grounding line migration. This necessitates the grounding line migration to be parameterized [*Barrand et al.*, 2013a].

Modeling the mechanically coupled ice sheet-ice shelf system is more desirable as it is a more physical-based modeling approach. However, there are currently a very limited number of plane view ice sheet models that are capable of modeling grounding line migration explicitly [e.g., *Winkelmann et al.*, 2011; *Pollard and DeConto*, 2012; *Cornford et al.*, 2013]. Of these models, even fewer have been used to run prognostic simulations under future climate scenarios [*Joughin et al.*, 2010]. This is mainly due to the issues outlined above and increasing levels of system uncertainty [*Vaughan and Arthern*, 2007]. Additionally, the required fine grid resolution at the grounding line ($\leq$100 m) [*Durand et al.*, 2009; *Cornford et al.*, 2013] and a lack of high-resolution input data (e.g., BEDMAP2 has a grid resolution of 1 km; [*Fretwell et al.*, 2013]) render modeling of the coupled ice sheet-ice shelf system for the APIS infeasible.

In the context of the rapid warming in the AP region, the ice dynamical response to ice shelf collapse has started to be a significant contributor to eustatic SLR. Based on climate projections, this SLR contribution may become even more important over the next centuries. In this paper, we compute the volume response of 210 ice shelf nourishing drainage basins (comprising ~62% of the area of the AP) following ice shelf collapse events. Ice shelf collapse timing is estimated from global climate model ensemble temperature projections for two different climate scenarios and grounding line retreat is parameterized using a new statistical model. In the absence of process-based predictions of ice shelf collapse timing, this series of scenario-based projections provides an estimate of the ice dynamical SLR from the APIS over the next 300 years. The projected SLR modeled by our experiments should be understood as an upper (−9°C isotherm) and lower bound (−5°C isotherm) for each simulation.

2. Methods

2.1. Ice Sheet Model Description

While the rugged topography of the AP might suggest the use of a full-system ice sheet model, the high computational cost and poorly known ice thickness distribution prevent such an application. Furthermore, in the absence of high-resolution input data, grounding line migration modeling will be beset by significant and compounding errors at every time step [*Schoof*, 2007]. Instead, a modeling framework and strategy are devised to utilize the best currently available ice sheet model of the APIS [*Barrand et al.*, 2013b], its constituent boundary condition data sets, and a statistical parameterization of grounding line retreat. The volume evolution of the grounded portion of the AP is modeled following imposition of an empirical-statistical estimate of grounding line retreat following ice shelf collapse (see section 2.3). The British Antarctic Survey Antarctic Peninsula Ice Sheet Model (BAS-APISM) is described in brief here, and the reader is referred to *Barrand et al.* [2013b] and references therein for a more detailed description of the model numerics.

BAS-APISM models ice flow by solving a linearized SIA equation, providing a scaling to the full Stokes equations. This approach is appropriate to the grounded ice portion of the APIS and permits low computational cost and a large ensemble of scenario calculations. The model is initialized using a combined altimetric and velocity initialization, taking advantage of the highest-quality observational boundary condition data sets [*Barrand et al.*, 2013b] and permitting a steady state starting condition. The use of a linearized diffusion-type ice sheet equation allows the flux perturbation equation to be solely ice flux based. This negates the need to estimate the rate factor or specify whether or not basal sliding is occurring. As ice thickness appears just once as a divisor in one term of the perturbation equation (equation (16) in *Barrand et al.* [2013b]) the linearized approach is less sensitive to errors in ice thickness than traditional SIA-based models. This is important for the AP where detailed ice thickness measurements are not always available [*Fretwell et al.*, 2013]. The linear nature of the flux perturbation equation also allows for superposable solutions, meaning that individual drainage basins can be modeled separately. SLR contributions from each modeled basin may then be summed to provide an ice sheet-wide contribution. BAS-APISM omits horizontal stress gradients (membrane-like stresses *Hindmarsh* [2009]) which is expected to introduce errors in SLR projections over the early decades following imposed grounding line retreat [*Williams et al.*, 2012]. These errors are expected to decay several decades after the perturbation [*Barrand et al.*, 2013b].

2.2. Climate Forcing

To estimate the timing of future ice shelf collapse, ensemble 2 m air temperature projections from 14 GCMs that participated in the Coupled Model Intercomparison Project Phase 5 [*Taylor et al.*, 2011] were used. Each GCM was forced using the emission scenarios "business as usual" (RCP4.5) and "high emission" (RCP8.5). Present-day temperature fields for the period 1979–2005 were represented by ERA-Interim climate reanalysis bilinearly interpolated to a $0.5 \times 0.5°$ grid. Following the bias correction approach of *Radic et al.* [2014], we shift the future monthly temperature time series for each GCM grid cell in the domain by the average bias for each month between the GCM and ERA-Interim temperatures over the period 1979–2005. In this way we corrected seasonality in the GCM temperatures relative to seasonality in the reanalysis. The bias-corrected GCM temperature fields were then bilinearly interpolated to the ice sheet model grid (900 m). It is important to note that ERA-Interim reanalysis temperature fields are not bias-free. *Jones and Lister* [2014] compared mean monthly ERA-Interim 2 m air temperature fields in Antarctica with mean monthly temperature records from 40 Antarctic weather stations and found that ERA-Interim displays a strong warm bias (up to 5°C) in the interior of the ice sheet and a cold bias in coastal areas (up to −6°C). For the AP, the picture is less homogeneous. At 6 of the 10 weather stations ERA-Interim shows a cold bias (up to −3.2°C) for the period 1979–2013 with an average cold bias for all 10 stations of −0.8°C.

In order to estimate ice shelf collapse timing, the empirically-based ice shelf viability limits, the −5°C mean annual isotherm and the −9°C mean annual isotherm, were tracked in the interpolated temperature fields. To allow for partial ice shelf collapse, the major fringing ice shelves were divided into subentities (see Figure 1), based on the N-S extent of each ice shelf. This results in one subdivision for Scar Inlet, two for Larsen C Ice Shelf, three for Larsen D Ice Shelf, three for George VI Ice Shelf, and one for Stange Ice Shelf (Figure 1).

To our knowledge, no publication has investigated the lag time between passing of the thermal limit of viability and collapse of the ice shelf. Thus, three timing scenarios were used to estimate the timing of future ice shelf collapse for the isotherms. Scenario 1 assumes immediate collapse of the ice shelf subentity,

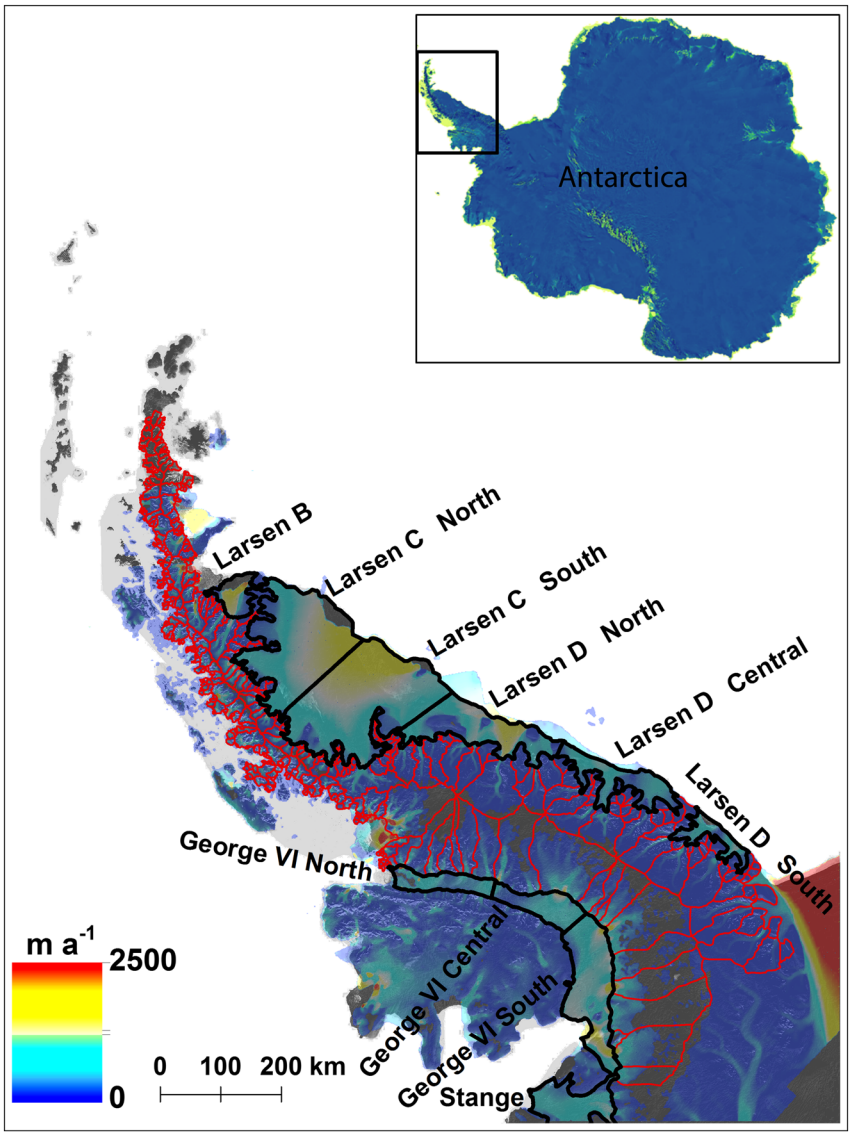

Figure 1. Landsat Image Mosaic of Antarctica (LIMA) of Antarctic Peninsula region (http://lima.usgs.gov/index.php) with surface ice velocity from *Rignot et al.* [2011] overlain. Red outlines depict 460 largest drainage basins, and black lines show ice shelf subdivisions. Map approximates ice sheet model domain. Lower left corner in polar stereographic coordinates is at −2611350, 239850 and upper right corner at −1304550, 1669050.

if the entire ice shelf subentity is located north of the respective limit of viability for one calendar year (no running mean scenario); Scenario 2 applies a 4 year running mean; and Scenario 3 applies an 8 year running mean. Scenarios 2 and 3 therefore require that the viability limit is south of the ice shelf subentity for 4 and 8 consecutive calendar years, respectively.

Mean annual temperature projections for the ice sheet model domain are shown in Figure 2. The range in mean annual temperature across the GCMs is large, with temperature differences in excess of 4°C due to a number of cold/warm GCM runs (Figures 2b and 2d). In particular, GFDL displays a strong cold bias in the RCP8.5 scenario compared to the rest of the GCMs (Figure 2b). Nevertheless, the ranges modeled across both projection periods and emission scenarios are very similar (standard deviation ~1.0°C), with the exception of Figure 2d where the range increases to 1.7°C. Air temperature projections show the expected steeper rise in the RCP8.5 scenario than in RCP4.5 (Figures 2b and 2d). For the GCMs spanning until 2300, the steepest temperature rise is observed in the 21st century before the rate of warming decreases during the latter two centuries (Figure 2d).

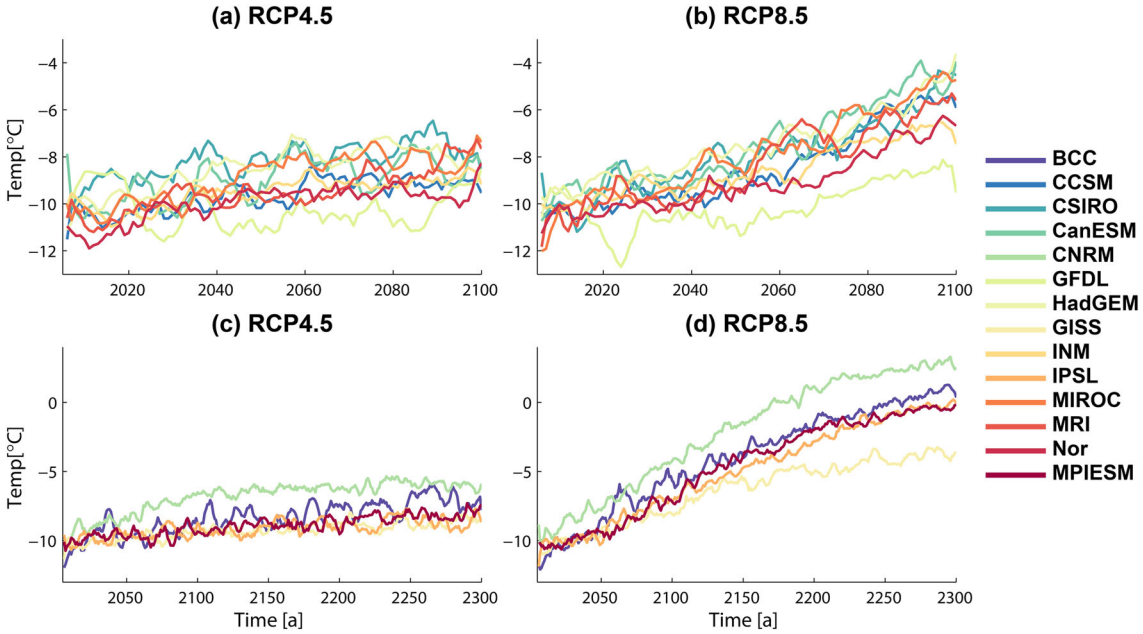

Figure 2. Smoothed (5 year running mean) mean annual 2 m air temperatures from 14 GCMs for ice sheet model domain. (top row) Temperatures to 2100 for the (a) "low-emission" and (b) "high-emission" scenarios. (bottom row) Temperatures to 2300 for the (c) "low-emission" and (d) "high-emission" scenarios. A full list of GCMs can be found under: http://cmip-pcmdi.llnl.gov/cmip5/citation.html.

Differences in mean annual temperatures also propagate into ice shelf collapse timing. There are significant differences in collapse timing within and across collapse timing scenarios. Predicted ice shelf collapse can vary by more than 100 years for some ice shelves (e.g., Figure 3d, Stange Ice Shelf). Typically, GCMs estimate similar ice shelf collapse timings up until 2050 from when they start to diverge, though this trend is not uniform

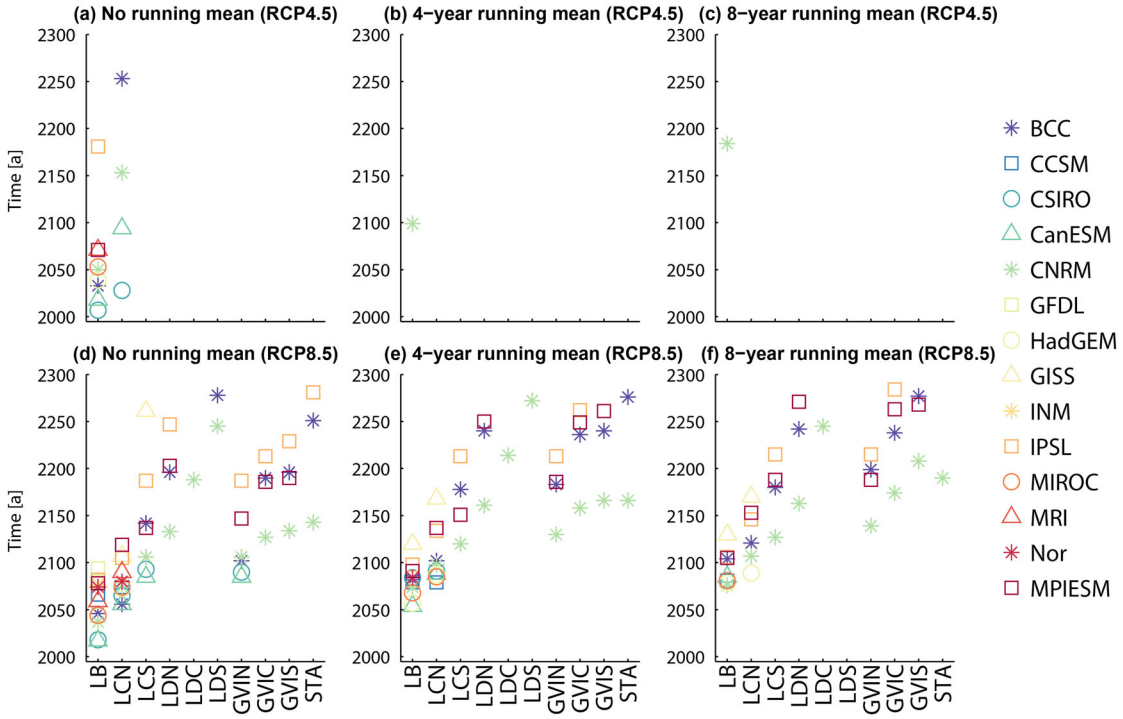

Figure 3. Ice shelf collapse timing derived using the −5°C isotherm for all 10 ice shelf entities. Ice shelf abbreviations are as follows: LB = Larsen B Ice Shelf, LCN = Larsen C Ice Shelf North, LCS = Larsen C Ice Shelf South, LDN = Larsen D Ice Shelf North, LDC = Larsen D Ice Shelf Central, LDS = Larsen D Ice Shelf South, GVIN = George VI Ice Shelf North, GVIC = George VI Ice Shelf Central, GVIS = George VI Ice Shelf South, STA = Stange Ice Shelf.

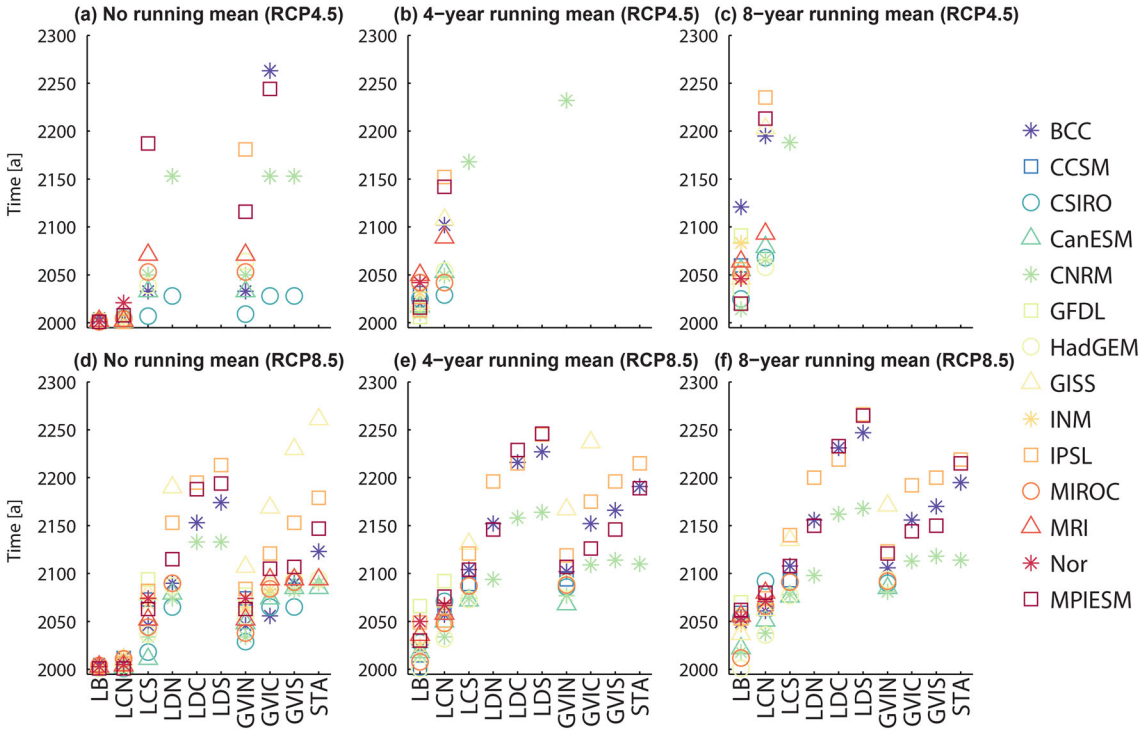

Figure 4. Ice shelf collapse timing derived using the −9°C isotherm for all 10 ice shelf entities. Ice shelf abbreviations are the same as in Figure 3.

across different scenarios. Judging from the ice shelf collapse timings in Figures 4d – 4f, the majority of the GCMs appear to capture the east-west temperature gradient across the AP (collapses are predicted earlier for ice shelves on the west coast compared to those at similar latitudes on the east coast).

2.3. Grounding Line Retreat Parameterization

This section describes the method used to estimate grounding line retreat for all ice shelf nourishing drainage basins in response to ice shelf collapse. In the first part, we develop a multivariate linear regression (MVLR) model and evaluate the model performance. In the second part, we use the results of our statistical model in conjunction with a simple speedup scenario of tributary glaciers following ice shelf collapse to estimate the final grounding line retreat for each individual drainage basin.

To map changes in grounding line position, two grounding line mapping products were used: (1) MOA [*Scambos et al.*, 2007] and (2) MEaSUREs [*Rignot et al.*, 2011]. For 189 of the mapped 193 drainage basins, there was a 8–10 year time differential between the data sets, allowing detection of positional changes between 1994 and 2004. Positional changes were mapped at five locations along each drainage basin front at equal

Table 1. List of Multivariate Linear Regression Predictor Variables for the AP Grounding Line Retreat Parameterization[a]

Predictor Variable	Variable Type	Class Type	Rank
Basin class	nonmetric	geometric	1
Ice shelf collapse	nonmetric	ice dynamical	2
Basin ice velocity	metric	ice dynamical	3
Basin front	nonmetric	geometric	4
Location	nonmetric	-	5
Bedrock slope	metric	ice dynamical	6
Ice thickness at grounding line	metric	ice dynamical	7
Bedrock elevation at grounding line	metric	ice dynamical	8
Basin size	metric	geometric	9

[a]Rank lists predictor variables in terms of their importance to overall model fit.

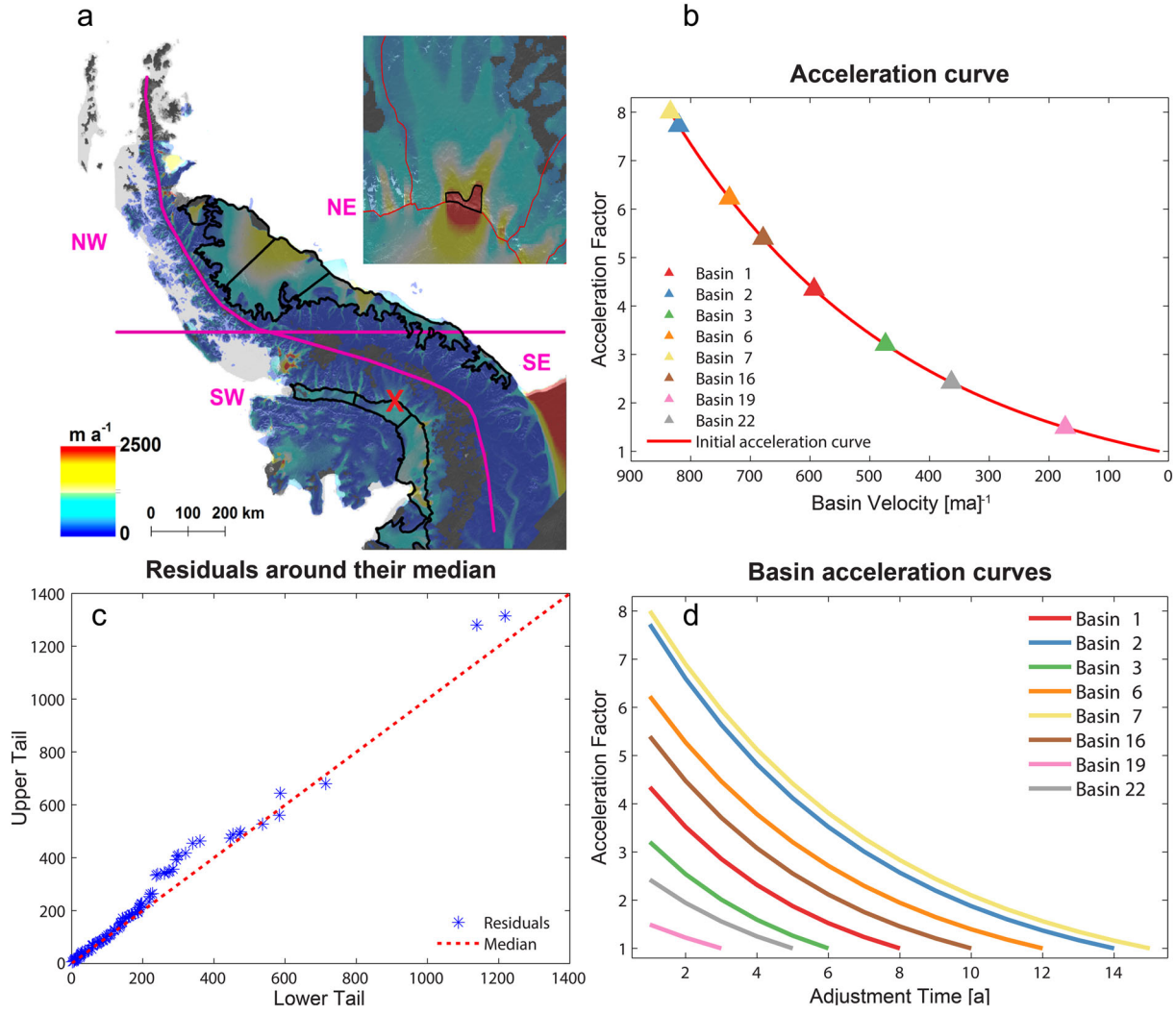

Figure 5. (a) Map as in Figure 1, including Location variable (pink). Red cross approximates location of inset map. Inset map shows sample drainage basin of area (black) used for velocity acceleration in statistical model. (b) Displays initial acceleration curve with triangles approximating the starting position of basin acceleration curves in (d). (c) Shows the distribution of residuals of the MVLR.

intervals and were then averaged. This was repeated for all 193 drainage basins. The mean positional change of these 193 drainage basins then served as the dependent variable for the statistical model. A range of independent variables was used to predict the value of the dependent variable. The selection of the predictor variables was based on observations from drainage basins of the AP presently adjusting to recent ice shelf removal [*Rott et al.*, 2014; *Scambos et al.*, 2014; *Cook et al.*, 2014] and on theoretical ice dynamical considerations [*Schoof*, 2007; *Goldberg et al.*, 2009], affecting grounding line position. Table 1 comprises a list of all the variables. The variables are divided into a geometric class and an ice dynamical class. Drainage basins presently adjusting to ice shelf removal have typically experienced larger grounding line retreat than other basins. Therefore, a variable whether or not ice shelf collapse occurred in between the grounding line mappings was included. In addition to this, a geographical variable ("Location") was included which divides the AP into four subregions (Figure 5a) and accounts for the reported spatially variable area loss of marine terminating glaciers in the AP region [*Cook et al.*, 2014; *Scambos et al.*, 2014].

Following ice shelf collapse, recent observations of the glaciers draining into the Prince-Gustav-Channel and the Larsen A embayment suggest the magnitude of the ice dynamic adjustment to be a function of glacier size, geometry, mass turnover, and subglacial topography [*Rott et al.*, 2014; *Scambos et al.*, 2014]. As shown by *Schoof* [2007], mass turnover of marine terminating outlet glaciers strongly depends on the ice thickness at the grounding line. The importance of the subglacial topography has also been demonstrated in theoretical

ice dynamical considerations [*Schoof*, 2007; *Goldberg et al.*, 2009], showing that for a two-dimensional marine ice sheet, there cannot be a stable grounding line position on reverse bed slopes, thus promoting sustained grounding line retreat. The "basin front" and "basin class" variables were derived from *Cook et al.* [2014] for the AP from 63 to 70°S and extended to all drainage basins south of 70°S. A detailed overview of individual drainage basin classes is provided by *Cook et al.* [2014]. The ice thickness at the grounding line, bedrock elevation at the grounding line, and bedrock slope were derived from *Huss and Farinotti* [2014] for the AP from 63–70°S and for all drainage basins south of 70°S from BEDMAP2 [*Fretwell et al.*, 2013]. Both data sets had previously been bilinearly interpolated onto the ice sheet model grid.

As outlined above, the position of the grounding line is affected by a range of variables. Multivariate linear regression allows examination of the relationship between this set of variables and a dependent variable (grounding line position). The statistical model has the form

$$Y = \alpha_0 + \beta_i X_i + \epsilon \qquad i = 1, \ldots, 9 \tag{1}$$

where α_0 is the intercept, β_i is the regression coefficient, X_i is a predictor variable, and ϵ is the residual or prediction error [*Hair et al.*, 1995]. Since some of the mapped changes in grounding line position may be erroneously large or small due to mislocation of the grounding line position of the mapping products, the regression was performed in a robust mode to reduce the effect of outliers on the results (for equations see Appendix A). Analysis of the residuals of our model reveals that the underlying assumptions of linearity, heteroscedasticity (presence of unequal variances), and the independence of the error terms are all complied by our MVLR [*Hair et al.*, 1995]. Residuals of the model are not strictly normally distributed but display a "thin tail" in their distribution pattern, violating the assumption of normality of the error term distribution. This means that for extreme values, the predicted values are significantly underestimated or overestimated. However, only a relatively small number of drainage basins (<20 basins) are affected by this (Figure 5c). The correlation is significant at the 1% level but with a relatively low R^2 value of 0.22. The corresponding standard error of the analysis is 219 m a^{-1}. We tested the relative importance of each individual predictor variable to the overall model fit by leaving out one by one predictor in the model and calculating how the correlation changes. This reveals that the most important predictor variables are basin class, "ice shelf collapse," and "ice velocity" (Table 1). However, up to rank 7, all variables contribute almost equally to the overall model fit. In comparison, the predictor variables "bedrock elevation at the grounding line" and "basin size" do not contribute significantly to the overall model fit. We still include them into our statistical model since we attribute their relative unimportance to the very heterogeneous glaciological setting in the AP, but they may be important locally. The quality of the model is significantly improved by only using the higher-resolution bedrock topography and ice thickness data from *Huss and Farinotti* [2014] for the northern AP (63°–70°S). In that case, the R^2 rises to 0.49 and the corresponding standard error reduces to 184 m a^{-1}. However, as there are almost no ice shelf nourishing drainage basins in this part of the AP, the results of the model would be skewed toward the other basin classes. To avoid this bias in our analysis, we rather accept the poorer model with less bias toward non-ice shelf nourishing drainage basins.

Given the annual positional changes estimated from the model, the following scenario is assumed for each of the 210 ice shelf nourishing drainage basins: In response to ice shelf removal, tributary outlet glaciers will show an immediate speedup. In the years following the initial acceleration, the outlet glaciers will slowly adjust to the new boundary conditions and the velocity acceleration will decay over time until pre-ice shelf collapse velocities are restored. Similar behavior has been reported from drainage basins flowing into the former Larsen A and Larsen B embayments [e.g., *Rott et al.*, 2002; *Scambos et al.*, 2011; *Rott et al.*, 2011; *Wuite et al.*, 2015]. The time period it takes for each drainage basin to adjust to the new boundary conditions is defined as the adjustment period. The initial speedup applied to each drainage basin is normalized on the basis of observations from outlet glaciers feeding into the former Larsen B Ice Shelf. *Rignot et al.* [2004] reported an eightfold outlet glacier velocity increase as maximum. Thus, we apply an eightfold initial velocity increase to the fastest flowing outlet glacier (820 m a^{-1}) and no acceleration to all drainage basins with velocities < 15 m a^{-1}. For all the drainage basins with velocities between these bounds, the initial velocity acceleration is determined by fitting an exponential function through the upper and lower bounds (Figure 5b). The length of the adjustment period was also normalized, applying a maximum of 15 years to the drainage basin with the fastest ice velocity and 1 year to drainage basins with velocities <15 m a^{-1}. For all drainage basins with velocities between these bounds, the adjustment period follows a linear curve fitted through the upper and lower bounds. The length

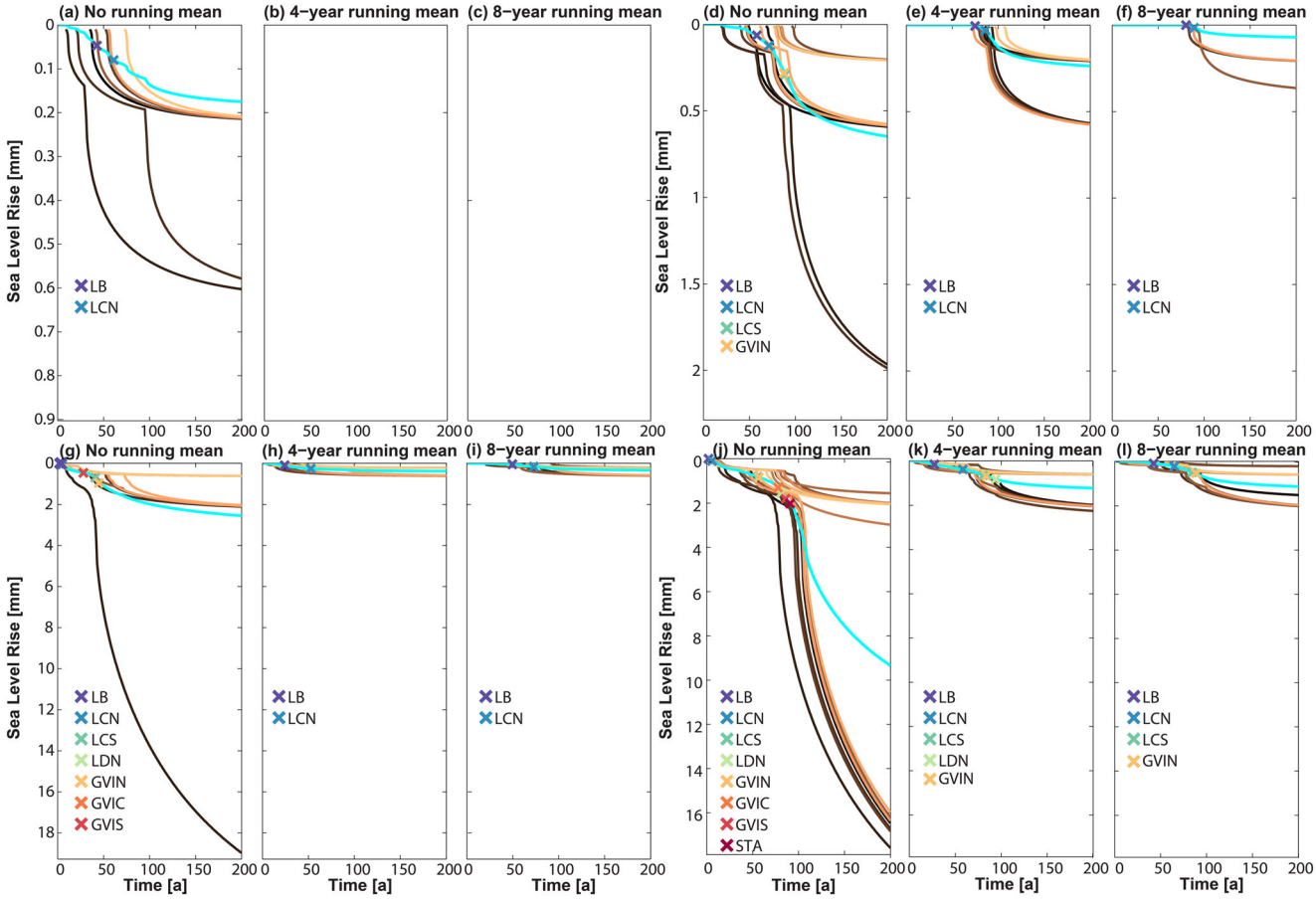

Figure 6. SLR curves to 2200, forced by using the -5°C isotherm (upper panel) and -9°C isotherm (lower panel) for emission scenarios RCP4.5 (left panel) and RCP8.5 (right panel). Crosses denote multimodel mean ice shelf collapse timings. Cyan line shows multimodel mean SLR curve.

of the adjustment period is reasonable, considering that recent observation from drainage basins formerly feeding into Larsen A Ice Shelf are still adjusting some 20 years after ice shelf disintegration [*Rott et al.*, 2014].

Given initial acceleration and length of adjustment period, an exponential function is fitted through these two endpoints for each individual drainage basins. The exponential function was used to account for non-linearities in the system. Figure 5d shows acceleration curves for a number of sample drainage basins. Total grounding line retreat rates are then calculated for each basin using the regression equation and multiplying the velocity coefficient by the calculated acceleration factor in each year. These annual retreat rates are then summed up to provide the final grounding line retreat. This method results in an average grounding line retreat of 1.4 km for all ice shelf nourishing drainage basins. The majority of the drainage basins show grounding line retreat less than 1 km, with five drainage basins showing total grounding line retreat >10 km and a maximum grounding line retreat of 42 km (basin 7).

2.4. Experimental Setup

As our GCM approach provides empirically-based ice shelf breakup timing estimates for two different time periods (2000–2200 and 2000–2300), two sets of simulations were performed. Experiment 1 included the ice shelf collapse timing of all 14 GCMs, allowing ice shelf breakup to occur until 2100. Following ice shelf breakup, each individual ice shelf-nourishing drainage basin was simulated until 2200, providing at least a century to adjust to the new boundary conditions. Experiment 2 included the ice shelf collapse timing of the 5 GCMs spanning to 2300 and allowing ice shelf breakup until 2300. Each ice shelf nourishing basin's response to the imposed grounding line retreat was then modeled until 2300, reducing the potential length of the adjustment period in comparison to Experiment 1. The grounding line retreat was readily imposed by instantaneously removing all grounded ice above sea level in the zones downstream of the prescribed new grounding line.

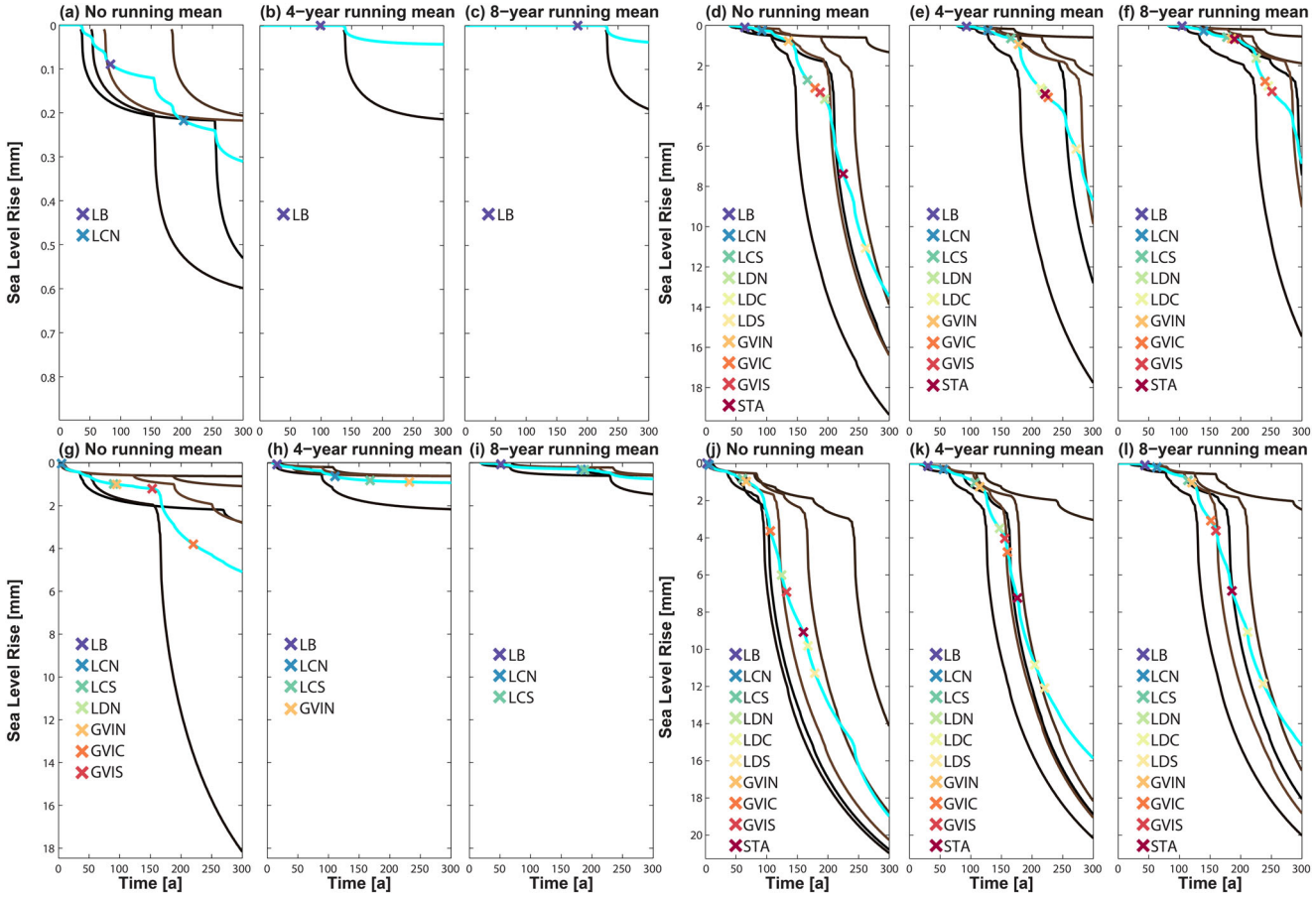

Figure 7. SLR curves to 2300, forced by using the -5°C isotherm (upper panel) and -9°C isotherm (lower panel) for emission scenarios RCP4.5 (left panel) and RCP8.5 (right panel). Crosses denote multimodel mean ice shelf collapse timings. Cyan line shows multimodel mean SLR curve.

As an instantaneous grounding line retreat is somewhat unrealistic, the same experiments were repeated enforcing a stepwise imposition of the estimated grounding line retreat. Using the annual retreat rates derived from the statistical model, grounding line retreat steps of 0.5, 1, 2, 3, 4, 5, 7.5, 10, 15, and 20 km were applied before the final maximum grounding line retreat was imposed. In addition to modeled changes to 2300, each drainage basin was simulated until it reached steady state. Here steady state is reached if the annual volume loss is <1% of the initial volume loss of the first year following ice shelf collapse (the period when volume losses are greatest).

3. Results

The ice dynamical response of 199 ice shelf nourishing drainage basins following ice shelf collapse was calculated. Eleven ice shelf-nourishing drainage basins were omitted from the analysis due to negligible expected grounding line retreat. Results from the stepwise grounding line retreat implementation are not presented as they showed almost identical results as the simulations with the instantaneous grounding line retreat implementation. This was because every drainage basin had at least 25 years to adjust to the grounding line perturbation, effectively eliminating the effect of this implementation.

3.1. Projected Sea Level Rise to 2200

SLR rise projections are highly variable across all scenarios in Experiment 1 and largely depend on the chosen thermal viability limit, emission scenario, and delay in ice shelf collapse (Figure 6). Differences range from zero SLR contribution (Figures 6b and 6c), to a maximum projected SLR for a single GCM run of ~18.0 mm SLE by the end of the forecast period (Figure 6g). Even within the same thermal viability limit, projected SLR differences are large (up to ~18.0 mm SLE). Across running mean scenarios, SLR projections differ in multimodel mean (cyan lines, Figures 7g–7i) as well as in variance (copper lines, Figures 7g–7i), even though there is an equal time interval between the running mean scenarios. In the model runs using the more conservative

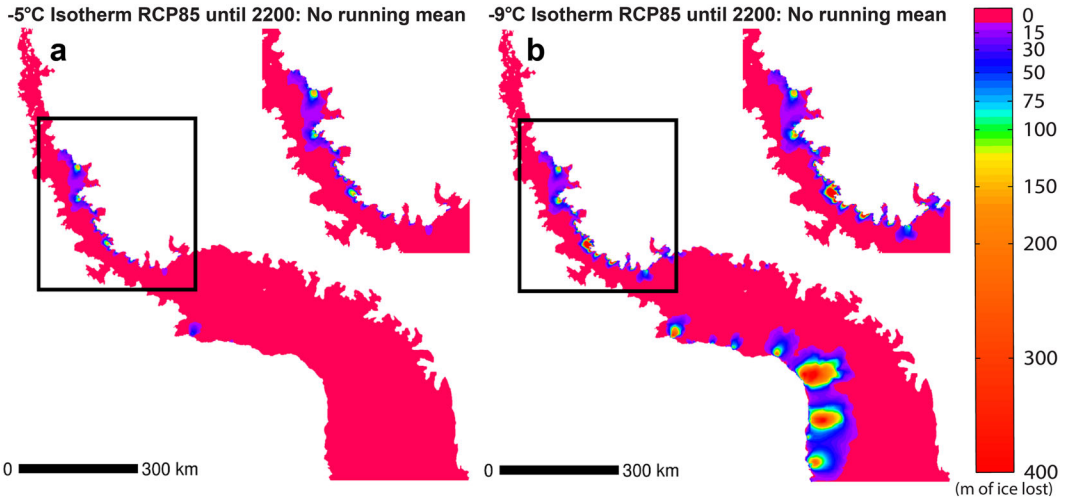

Figure 8. Multimodel mean thinning pattern using the high-emission scenario and (a) the −5°C isotherm and (b) −9°C isotherm. Black boxes approximate location of inset map.

−5°C isotherm and the low-emission scenario (RCP4.5; Figures 6a–6c), only six GCM runs predict any ice shelf breakup before 2100. The multimodel mean SLR contribution is ~0.2 mm SLE (Figure 6a). This number more than doubles to ~0.6 mm SLE in the high-emission scenario, with projected SLR from individual GCM runs as high as ~2 mm SLE (Figure 6d). This underlines the importance of the choice of GCM run in projecting SLR. The SLR curves in Figure 6d have up to three distinct steps, each marking the response to an ice shelf breakup event. The rate of change in the SLR curve initiated by ice shelf breakup, however, is not equidistant, showing that the SLR contribution will vary between individual ice shelves. This is caused by the differing grounding line retreat imposed on each basin and the differing number of drainage basins affected by the respective ice shelf breakup event.

The less conservative −9°C isotherm as the thermal viability limit provides higher SLR projections. The projections from the low emission scenario (Figures 6g–6i) approximately follow the projected SLR using the high-emission scenario and the −5°C isotherm (Figures 6a–6c). However, one GCM run predicts the collapse of the entire George VI Ice Shelf system, thus a SLR that is approximately tenfold higher than in any other GCM forcing (Figure 6g). This only occurs in the no running mean scenario, indicating a short (<4 years) but very warm period in that GCM run.

Similar SLR projections are evident in the high-emission scenario but across the majority of GCM runs (Figures 6j–6l). Ice shelf collapse of all but two Larsen D Ice Shelf entities is projected, raising the multimodel mean projection to ~10 mm SLE by the end of the forecast period (year 2200). The number of projected ice shelf breakup events decreases with longer delay in ice shelf collapse, and this leads to much reduced SLR projections (e.g., Figures 6j–6l).

3.2. Projected Sea Level Rise to 2300

Results from Experiment 2 show a similar spread in projected SLR as in Experiment 1, ranging from ~0.2 mm SLE to ~19 mm SLE (Figure 7, copper lines). However, when corresponding scenarios are compared, projected SLR in Experiment 2 are larger. This is due to the extended simulation period allowing ice shelf breakup to occur until 2300, though a reduction in participating GCM runs could also affect SLR projections by filtering out the extreme members, leading to a better consensus in SLR projection across GCM runs. Figures 7d–7f suggests the former, as SLR curves do not start to lower before 2200. The difference in SLR projections between Experiments 1 and 2 varies, corroborating the particular (un)importance of certain ice shelves, e.g., in the low-emission scenario using the −5°C isotherm, projected SLR is similar (Figures 6a–6c and 7a–7c), whereas in the high-emission scenario, projected SLR is approximately tenfold higher in Experiment 2 (Figures 6d–6f and 7d–7f).

3.3. Relevance of Removed Grounded Ice

Not all of the projected SLR in Experiments 1 and 2 result from ice dynamic thinning following ice shelf collapse but is in fact a result of grounded ice being removed when the grounding line retreat is applied. By design,

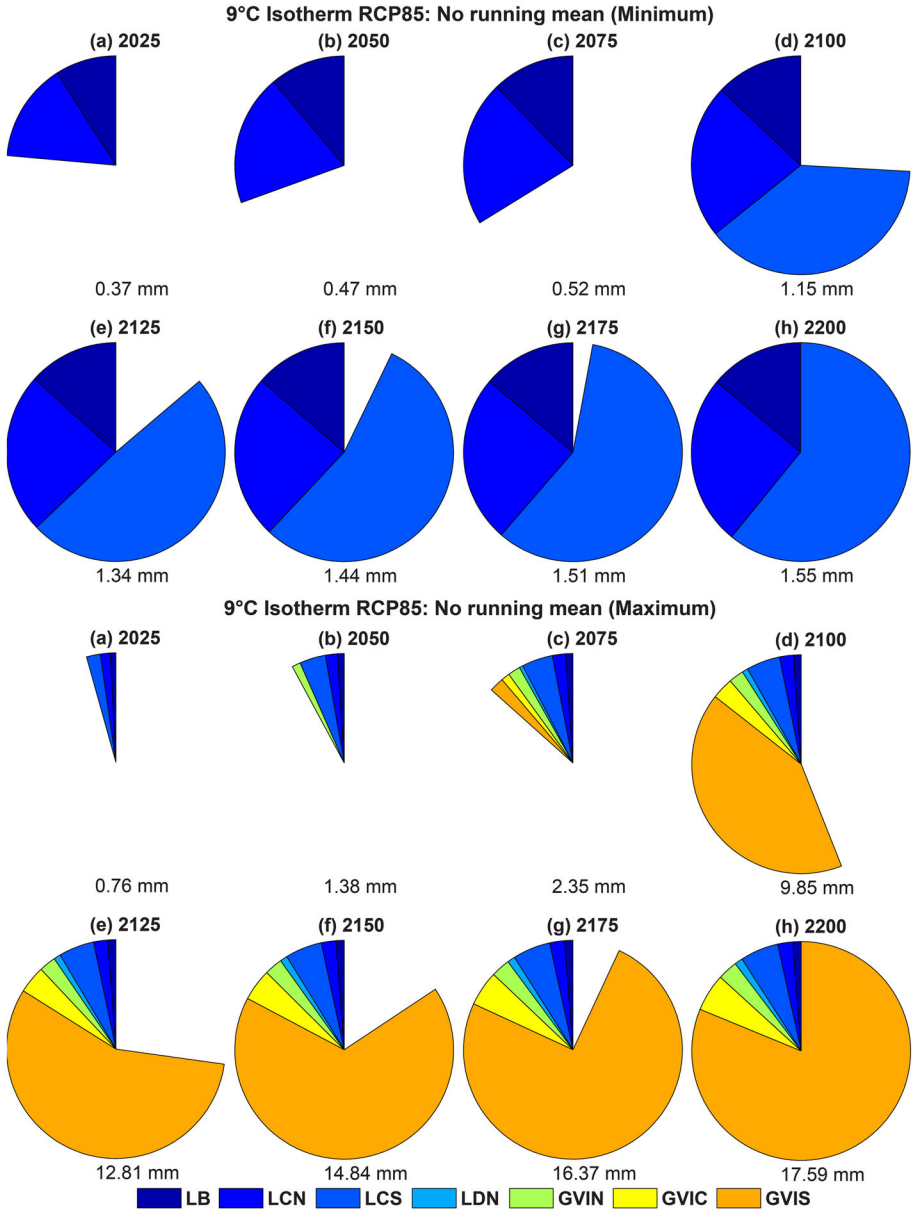

Figure 9. Temporal partitioning of SLR from the coldest (top) and warmest (bottom) GCM runs to 2200, using the −9°C isotherm high-emission scenario with no running mean.

grounding line retreat is imposed by instantaneously removing all grounded ice above sea level in the zones downstream of the prescribed new grounding line. As this ice is grounded at the time of removal, this arguably contributes to overall SLR. We tested the importance of this process by using the coldest and warmest GCM runs of Experiments 1 and 2 and calculating the relative contribution of grounded ice removal to the overall SLR. Results show that the relative importance varies, accounting between 8.3% and 23.8% of the overall SLR. Higher percentages occur for smaller overall projected SLR but significantly decrease (~9–10%) for SLR >10 mm SLE. If the maximum grounding line retreat is applied to each drainage basin, the contributions of grounded ice removal is ~1.7 mm SLE.

3.4. Regional Ice Dynamic Thinning Pattern

Ice dynamical thinning patterns are shown in Figure 8. In the −5°C isotherm simulations, ice dynamic thinning is limited to the northern part of the AP (Graham Land) (Figure 8a). Thinning rates are large locally (up to 442 m ice lost) but diminish quickly inland. However, thinning does propagate as far inland as ~54 km. If mass loss caused by ice dynamic thinning was equally distributed over the APIS, it would thin the entire ice

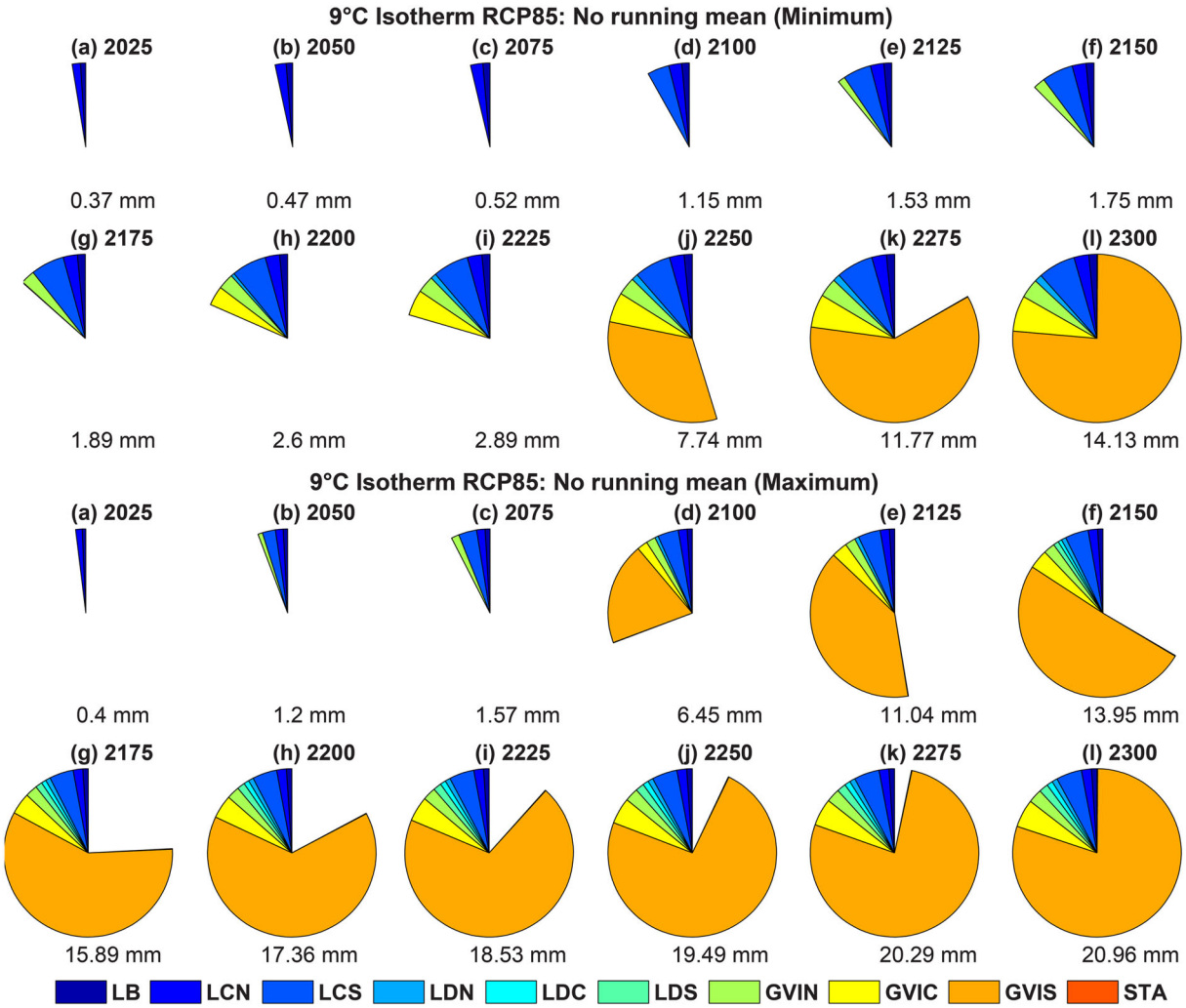

Figure 10. Temporal partitioning of SLR from the coldest (top) and warmest (bottom) GCM runs to 2300, using the -9°C isotherm high-emission scenario with no running mean.

sheet at a rate of 0.01 m a^{-1} over the next 200 years. In the −9°C isotherm scenario, a similar thinning pattern is modeled in Graham Land. However, widespread thinning in excess of 200 m of ice lost (up to 492 m ice lost) occurs in the southern AP (Figure 8b). If the mass loss due to ice dynamic thinning was equally distributed over the APIS for the −9°C isotherm scenario, it would thin the entire ice sheet at a rate of 0.04 m a^{-1} over the next 200 years. Thinning is also not limited to coastal areas but is transmitted much farther upstream in the southern AP, reaching a maximum inland extent of ~136 km. Upstream of grounding lines along disintegrated ice shelves, thinning becomes more continuous, spreading well over the boundaries of drainage basins. This leads to coalescence of individual thinning patches and thus a more continuous thinning pattern (Figure 8b).

3.5. Temporal Partitioning of Sea Level Rise

In order to assess the importance of ice shelf entities, SLR contributions are split into intervals of 25 years for each individual ice shelf. If all ice shelves were to disintegrate, the two largest contributions to overall SLR are George VI Ice Shelf Central and George VI Ice Shelf South (Figures 9, 10). George VI Ice Shelf South comprises >75% of the total projected SLR in this scenario. However, in the first century of the simulation period, SLR contributions are evenly spread among the other ice shelves (Figures 9, 10).

The observed spread in projected SLR between the warmest and coldest GCM run can be large (Figure 9), with the maximum projected SLR approximately elevenfold higher than the minimum. This is unsurprising considering the importance of George VI Ice Shelf South and that it does not disintegrate in the coldest GCM (Figure 9). Drainage basins react quickly to the imposed grounding line perturbation and SLR contributions are highest in the first decade following ice shelf collapse before mass losses begin to slow down

(Figures 9 and 10). Even though the rate of SLR decreases in subsequent time steps (Figures 9 and 10), they do not reach steady state by the end of the simulation period.

3.6. Steady State Sea Level Rise Simulations

Most SLR curves still display a rather steep slope at the end of the simulation period, indicating that drainage basins have not yet fully adjusted to the new imposed boundary conditions (Figure 7). To derive a maximum potential SLR from the imposed grounding line retreat, each drainage basin was modeled to steady state (as defined in section 2.4). The experiment shows that 145 drainage basins did not reach steady state conditions within 100 years after imposition of the grounding line perturbation. The mean adjustment period for all drainage basins is 175 years after imposition of the grounding line perturbation, with adjustment periods as long as 602 years. The length of the adjustment period seems to be not only a function of the magnitude of the perturbation but also a function of ice velocity, as the longest adjustment periods are almost evenly distributed between basins with either slow ice velocities or large imposed grounding line perturbations. If all individual contributions are summed, steady state SLR amounts to ~24.6 mm SLE, ~1.7 mm SLE more than the maximum projected SLR from any of the simulations in Experiments 1 and 2.

4. Discussion

Projected SLR depends on a number of factors in our simulations, including the following: delay in ice shelf collapse, emission scenario, the thermal limit of viability, and the quality of the input data. Therefore, the projected SLR modeled by these experiments should serve as an upper and lower bound for the more conservative −5°C isotherm threshold and the less conservative −9°C isotherm threshold, respectively. The most representative SLR projections for each simulation are provided by the multimodel means (cyan lines in Figures 6 and 7). The multimodel means for the no running mean simulations range from 0.19 mm SLE to 9.4 mm SLE in Experiment 1 and 0.31 mm SLE to 19 mm SLE in Experiment 2. If an ice density of 917 kg m^{-3} is assumed, this translates to a range of 69 Gt (0.35 Gt a^{-1}) to 3403 Gt (17 Gt a^{-1}) of ice lost for Experiment 1 and 112 Gt (0.37 Gt a^{-1}) to 6878 Gt (22.9 Gt a^{-1}) of ice lost for Experiment 2. For comparison, Pine Island Glacier in West Antarctica lost ice at a rate of ~20 Gt a^{-1} between 1992 and 2011 [*Shepherd et al.*, 2012] and the APIS as a whole lost mass at a rate of 24 ± 18 Gt a^{-1} between 2010–2013 [*McMillan et al.*, 2014]. This means that the multimodel mean in the high-emission scenarios of Experiments 1 and 2 provides a similar range as the entire contemporary mass loss of the APIS. However, projected mass loss from individual GCM runs may exceed these values and project possible mass loss rates as high as 34.7 Gt a^{-1} over the next 200–300 years, from ice dynamic thinning alone. Although the model spread in Experiments 1 and 2 provide an estimate of the uncertainties bars associated with the multimodel means, we discuss below the main sources of uncertainties in our experiments.

4.1. Timing of Ice Shelf Collapse

The ice shelf collapse timing estimated from GCM runs using the pair of thermal viability limits reproduces the temperature pattern of the AP rather well. Given the prevalent east-west temperature divide in the AP [e.g., *Morris and Vaughan*, 2003], it is expected that ice shelves on the western side of the AP will disintegrate earlier than their counterparts on the eastern side at the same latitude. This pattern is captured throughout the GCM runs despite their initial coarse spatial resolution.

Although the concept of a thermal viability limit for ice shelves dates back to the 1970s [*Mercer*, 1978], little has been published on the time delay between passing of the thermal viability limit and ice shelf disintegration. The length of the delay in the experiments is arbitrary but leads to significant changes in the estimated ice shelf collapse timing (>50 years for some GCM runs). Most pronounced are these changes from scenario 1 (no time delay) to scenario 2 (4 year running mean). Despite the southward migration of the thermal viability limits, this migration does not occur gradually but by step changes north or south from year to year. In some instances this may cause an early collapse in scenario 1 (Figure 6g) but no collapse in scenarios 2 and 3. Scenarios 2 and 3 provide more robust forecasts by being resistant to short (≤4 years) anomalously warm periods. An important step toward improved future SLR projection efforts would be to include a more physically-based breakup mechanism.

To further test the robustness of the ice shelf thermal viability tracking, we used the data from the ERA-Interim period 1979–2010 to estimate collapse timings of previous ice shelf breakup events. During the ERA-Interim period four ice shelves in the AP disintegrated: Prince Gustav Ice Shelf (1995); Larsen Inlet Ice Shelf (1989);

Larsen A Ice Shelf (1995); and Larsen B Ice Shelf (2002) [e.g., *Rott et al.*, 1996; *Scambos et al.*, 2000, 2004]. Using the same method as in our GCM projections, the results show that the −5°C isotherm does not model any collapse across all three running mean scenarios during that period. In comparison, the −9°C isotherm suggests collapse of all four ice shelves in 1979 in scenario 1 (no running mean), collapse of Prince Gustav Ice Shelf and Larsen Inlet Ice Shelf in 1979 in scenario 2, and no ice shelf collapse in scenario 3.

It is somewhat unsurprising that this method is incapable of estimating the exact ice shelf collapse timing, considering that the ERA-Interim temperature data are beset by a considerable bias in the AP region [*Jones and Lister*, 2014]. In the light of that, these results indicate that the −9 isotherm should be understood as a pessimistic scenario and the −5 isotherm as an optimistic scenario to estimate ice shelf collapse. The actual collapse timing might lie somewhere in between these bounds. This is supported by the analysis of ERA-Interim temperature fields at the time of actual ice shelf collapse, revealing an averaged mean annual temperature over the four ice shelves of −8.2°C. Instead of the thermal viability limits used in this paper, this new temperature threshold might be used as ice shelf viability limit in future modeling experiments.

4.2. Grounding Line Parameterization

Despite including a variety of geometrical and ice dynamical variables into the statistical model, the overall model fit may be improved. We attribute this to a combination of the low accuracy of the mapped positional changes and the poor spatial resolution of input data (e.g., bedrock topography and ice thickness). However, where higher-resolution input data were used [*Huss and Farinotti*, 2014], significant gains in the goodness of the fit were demonstrated. Nonetheless, grounding line perturbation estimates derived from the model lie within a plausible range (0–45 km). Basing the expected grounding line retreat on velocity leads to large grounding line perturbation for all large and fast moving glaciers. This may result in an overemphasizing of ice velocity at the expense of other important ice dynamical attributes such as ice thickness at the grounding line and bedrock slope. However, it is a necessary outcome of the quality and availability of input data to the statistical model. The relative importance of George VI Ice Shelf, which is based on approximately threefold higher ice velocities than in any other drainage basins, may be overvalued in the experiments.

To investigate the sensitivity of the grounding line retreat estimates to different acceleration factors, we perturbed the initial velocity acceleration by −20% and +20% in our speedup scenario. The results of the sensitivity simulations provide very similar grounding line retreat estimates compared to our reference simulation. The average grounding line retreat is 1.4 km, and five drainage basins show a grounding line retreat >10 km for all three simulations. The most notable difference is in the maximum grounding line retreats which are 35 km and 48 km for −20% and +20%, respectively (42 km for reference simulation).

We chose the −9°C isotherm RCP8.5 model run to test how much these differences affect our SLR projections. Instead of using our reference grounding line retreat estimates, we force our ice sheet model by using the perturbed grounding line retreat estimates. Since this model run shows the highest SLR projections, it provides the maximum uncertainty associated with our grounding line retreat estimates. For the model runs to 2200, the differences in mean SLR projection are between 0.1 mm to 2.3 mm SLE (7% to 15%) with larger differences being modeled for larger mean SLR projections (Figure 6j). As mean SLR projections for the model runs to 2300 are larger than in the 2200 equivalent, absolute differences in mean SLR projections increase, ranging from 1.3 mm to 3.1 mm SLE, but relative differences show a very similar range of 9% to 16%.

Using the perturbed grounding line retreat estimates, we also investigated their effects on the adjustment period (the time it takes for drainage basins to reach steady state). Steady state is reached if the annual volume loss is <1% of the initial volume loss of the first year following ice shelf collapse. The effects are negligible as mean adjustment times for all drainage basins vary by 0.7 to 1.2 years (0.4% to 0.7%), while minimum adjustment time (12 years) and maximum adjustment time (602 years) are unaffected.

To further test the capabilities of the statistical model, we used the model to try and reproduce the grounding line retreat rates experienced by drainage basins formerly feeding Larsen B Ice Shelf. Our mean computed grounding line retreat rate of ∼4.5 km agrees well with retreat rates derived from observations [*Riedl et al.*, 2004; *Rott et al.*, 2007]. Satellite observations show that drainage basins of Hektoria and Crane glaciers have experienced the most dramatic grounding line retreat [e.g., *Wuite et al.*, 2015]. This pattern is reproduced by our statistical model which computes grounding line retreats of 56 km and 5 km for Hektoria and Crane glaciers, respectively. That the computed retreat rates do not match retreat rates from satellite observations is

expected as we use input data (e.g., velocity, ice thickness, and bedrock topography) that was acquired years after the collapse of Larsen B Ice Shelf.

5. Conclusions

We have modeled the response of 199 ice shelf nourishing drainage basins to ice shelf collapse and subsequent grounding line retreat in the AP over the next 200–300 years. A total of 14 GCM projections with two emission scenarios and two thermal viability limits were used to estimate the timing of future ice shelf collapse. The magnitude of the expected grounding line retreat following ice shelf collapse was derived, using a statistical model and assuming immediate speedup of tributary glaciers in response to ice shelf collapse. Our modeling experiments have led to the following main conclusions:

1. Empirically-based ice shelf collapse timing estimates vary across GCMs, emission scenarios, chosen thermal viability limits, and timing of delay in ice shelf collapse. While timing differences across GCMs, emission scenarios, and chosen thermal viability limits were expected, our experiments reveal that the time lag between passing of the viability limit and actual disintegration of the ice shelf introduces differences in the timing of collapse of >50 years. As the collapse timing determines the timing of the application of the grounding line perturbation, these differences propagate into the SLR projections, leading to a range of SLR projections for both experiments.
2. Owing to the application of a scenario-based approach to our simulations, each experiment provides a range of SLR projections. The most representative SLR projections for each simulation are provided by the multimodel means. Multimodel means project SLR between 0 mm to 9.4 mm SLE to 2200 for Experiment 1 and 0.04 mm to 19 mm SLE to 2300 for Experiment 2.
3. Major SLR projections are modeled in the years following ice shelf collapse before they start to decay. The magnitude of the decay strongly depends on the applied grounding line perturbation. In our simulations, drainage basins feeding into George VI Ice Shelf are by far contributing the most to overall SLR projections. Ice dynamic thinning in this region propagates as much as ~135 km upstream of the initial grounding line position, whereas in the northern AP (Graham Land) thinning is limited to areas in the immediate vicinity of the initial grounding line.
4. Annual mass loss projected from ice dynamic simulations of the high-emission scenario over the next 200–300 years are in a similar range to the contemporary mass loss of the APIS derived from satellite observations, underlining the importance of the ice dynamic component to SLR on the centennial time scale.

Appendix A: Weight Function Computation

The robust mode assigns a weight based on the bisquare weighting function

$$w = (\mathrm{abs}(r) < 1) \times (1 - r^2)^2 \tag{A1}$$

where value r in the weight function is

$$r = \mathrm{resid}/(\mathrm{tune} \times s \times \sqrt{1 - h}) \tag{A2}$$

Here tune = 4.685, resid is the vector of residuals from the previous iteration, h is the vector of leverage values from a least squares fit, and s is an estimate of the standard deviation of the error term computed by

$$s = \mathrm{MAD}/0.6745 \tag{A3}$$

where MAD is the median absolute deviation of the residuals from their median.

Acknowledgments
C.S. was supported by a PhD studentship from the University of Birmingham. The computations described in this paper were performed using the University of Birmingham's BlueBEAR HPC service, which provides a High Performance Computing service to the University's research community. See http://www.birmingham.ac.uk/bear for more details. We thank an anonymous reviewer and Ted Scambos for their comments which improved the manuscript.

References

Barrand, N. E., D. G. Vaughan, N. Steiner, M. Tedesco, P. Kuipers Munneke, M. R. van den Broeke, and J. S. Hosking (2013a), Trends in Antarctic Peninsula surface melting conditions from observations and regional climate modeling, *J. Geophys. Res. Earth Surf.*, *118*, 315–330, doi:10.1029/2012JF002559.

Barrand, N. E., et al. (2013b), Computing the volume response of the Antarctic Peninsula ice sheet to warming scenarios to 2200, *J. Glaciol.*, *59*(215), 397–409, doi:10.3189/2013JoG12J139.

Brunt, K. M., H. A. Fricker, L. Padman, T. A. Scambos, and S. O'Neel (2010), Mapping the grounding zone of the Ross Ice Shelf, Antarctica, using ICESat laser altimetry, *Ann. Glaciol.*, *51*(55), 71–79, doi:10.3189/172756410791392790.

Cook, A., D. Vaughan, A. Luckman, and T. Murray (2014), A new Antarctic Peninsula glacier basin inventory and observed area changes since the 1940s, *Antarct. Sci.*, *26*(Special Issue 6), 614–624, doi:10.1017/S0954102014000200.
Cook, A. J., and D. G. Vaughan (2010), Overview of areal changes of the ice shelves on the Antarctic Peninsula over the past 50 years, *Cryosphere*, *4*(1), 77–98, doi:10.5194/tc-4-77-2010.
Cook, A. J., A. J. Fox, D. G. Vaughan, and J. G. Ferrigno (2005), Retreating glacier fronts on the Antarctic Peninsula over the past half-century, *Science*, *308*(5721), 541–544, doi:10.1126/science.1104235.
Cornford, S. L., D. F. Martin, D. T. Graves, D. F. Ranken, A. M. Le Brocq, R. M. Gladstone, A. J. Payne, E. G. Ng, and W. H. Lipscomb (2013), Adaptive mesh, finite volume modeling of marine ice sheets, *J. Comput. Phys.*, *232*(1), 529–549, doi:10.1016/j.jcp.2012.08.037.
Corr, H. F. J., C. S. M. Doake, A. Jenkins, and D. G. Vaughan (2001), Investigations of an "ice plain" in the mouth of Pine Island Glacier, Antarctica, *J. Glaciol.*, *47*(156), 51–57, doi:10.3189/172756501781832395.
De Angelis, H., and P. Skvarca (2003), Glacier surge after ice shelf collapse, *Science*, *299*(5612), 1560–1562, doi:10.1126/science.1077987.
Durand, G., O. Gagliardini, T. Zwinger, E. Le Meur, and R. C. A. Hindmarsh (2009), Full stokes modeling of marine ice sheets: Influence of the grid size, *Ann. Glaciol.*, *50*(52), 109–114, doi:10.3189/172756409789624283.
Fretwell, P., et al. (2013), Bedmap2: Improved ice bed, surface and thickness datasets for Antarctica, *Cryosphere*, *7*(1), 375–393, doi:10.5194/tc-7-375-2013.
Fricker, H. A., R. Coleman, L. Padman, T. A. Scambos, J. Bohlander, and K. M. Brunt (2009), Mapping the grounding zone of the Amery Ice Shelf, East Antarctica using InSAR, MODIS and ICESat, *Antarct. Sci.*, *21*(5), 515–532, doi:10.1017/S095410200999023X.
Fyke, J. G., L. Carter, A. Mackintosh, A. J. Weaver, and K. J. Meissner (2010), Surface melting over ice shelves and ice sheets as assessed from modeled surface air temperatures, *J. Clim.*, *23*(7), 1929–1936, doi:10.1175/2009JCLI3122.1.
Goldberg, D., D. M. Holland, and C. Schoof (2009), Grounding line movement and ice shelf buttressing in marine ice sheets, *J. Geophys. Res.*, *114*, F04026, doi:10.1029/2008JF001227.
Hair, J. F., B. Black, R. Anderson, and R. Tatham (1995), *Multivariate Data Analysis With Readings*, 4th ed., Prentice-Hall, Inc., New Jersey.
Hindmarsh, R. C. A. (2004), A numerical comparison of approximations to the Stokes equations used in ice sheet and glacier modeling, *J. Geophys. Res.*, *109*, F01012, doi:10.1029/2003JF000065.
Hindmarsh, R. C. A. (2009), Consistent generation of ice-streams via thermo-viscous instabilities modulated by membrane stresses, *Geophys. Res. Lett.*, *36*, L06502, doi:10.1029/2008GL036877.
Hock, R., M. de Woul, V. Radic, and M. Dyurgerov (2009), Mountain glaciers and ice caps around Antarctica make a large sea-level rise contribution, *Geophys. Res. Lett.*, *36*, L07501, doi:10.1029/2008GL037020.
Holland, P. R., A. Jenkins, and D. M. Holland (2008), The response of ice shelf basal melting to variations in ocean temperature, *J. Clim.*, *21*(11), 2558–2572, doi:10.1175/2007JCLI1909.1.
Holland, P. R., H. F. J. Corr, H. D. Pritchard, D. G. Vaughan, R. J. Arthern, A. Jenkins, and M. Tedesco (2011), The air content of Larsen Ice Shelf, *Geophys. Res. Lett.*, *38*, L10503, doi:10.1029/2011GL047245.
Holland, P. R., A. Brisbourne, H. F. J. Corr, D. McGrath, K. Purdon, J. Paden, H. A. Fricker, F. S. Paolo, and A. H. Fleming (2015), Oceanic and atmospheric forcing of Larsen C Ice-Shelf thinning, *Cryosphere*, *9*(3), 1005–1024, doi:10.5194/tc-9-1005-2015.
Horgan, H. J., and S. Anandakrishnan (2006), Static grounding lines and dynamic ice streams: Evidence from the Siple Coast, West Antarctica, *Geophys. Res. Lett.*, *33*, L18502, doi:10.1029/2006GL027091.
Huss, M., and D. Farinotti (2014), A high-resolution bedrock map for the Antarctic Peninsula, *Cryosphere*, *8*(4), 1261–1273, doi:10.5194/tc-8-1261-2014.
Hutter, K. (1983), *Theoretical Glaciology: Material Science of Ice and the Mechanics of Glaciers and Ice Sheets*, vol. 1, Springer, Netherlands.
Jacob, T., J. Wahr, W. T. Pfeffer, and S. Swenson (2012), Recent contributions of glaciers and ice caps to sea level rise, *Nature*, *482*(7386), 514–518, doi:10.1038/nature10847.
Jansen, D., A. J. Luckman, A. Cook, S. Bevan, B. Kulessa, B. Hubbard, and P. R. Holland (2015), Brief communication: Newly developing rift in Larsen C Ice Shelf presents significant risk to stability, *Cryosphere*, *9*(3), 1223–1227, doi:10.5194/tc-9-1223-2015.
Jenkins, A., and S. Jacobs (2008), Circulation and melting beneath George VI Ice Shelf, Antarctica, *J. Geophys. Res.*, *113*, C04013, doi:10.1029/2007JC004449.
Jones, P. D., and D. H. Lister (2014), Antarctic near-surface air temperatures compared with ERA-Interim values since 1979, *Int. J. Climatol.*, *35*(7), 1354–1366, doi:10.1002/joc.4061.
Joughin, I., B. E. Smith, and D. M. Holland (2010), Sensitivity of 21st century sea level to ocean-induced thinning of Pine Island Glacier, Antarctica, *Geophys. Res. Lett.*, *37*, L20502, doi:10.1029/2010GL044819.
Kuipers Munneke, P., S. R. M. Ligtenberg, M. R. Van Den Broeke, and D. G. Vaughan (2014), Firn air depletion as a precursor of Antarctic ice-shelf collapse, *J. Glaciol.*, *60*(220), 205–214, doi:10.3189/2014JoG13J183.
Kulessa, B., D. Jansen, A. J. Luckman, E. C. King, and P. R. Sammonds (2014), Marine ice regulates the future stability of a large Antarctic ice shelf, *Nat. Commun.*, *5*, 3707, doi:10.1038/ncomms4707.
Luckman, A., A. Elvidge, D. Jansen, B. Kulessa, P. Kuipers Munneke, J. King, and N. E. Barrand (2014), Surface melt and ponding on Larsen C Ice Shelf and the impact of foehn winds, *Antarct. Sci.*, *26*(Special Issue 06), 625–635, doi:10.1017/S0954102014000339.
McMillan, M., A. Shepherd, A. Sundal, K. Briggs, A. Muir, A. Ridout, A. Hogg, and D. Wingham (2014), Increased ice losses from Antarctica detected by CryoSat-2, *Geophys. Res. Lett.*, *41*, 3899–3905, doi:10.1002/2014GL060111.
Mercer, J. H. (1978), West Antarctic ice sheet and CO_2 greenhouse effect: A threat of disaster, *Nature*, *271*(5643), 321–325, doi:10.1038/271321a0.
Meredith, M. P., and J. C. King (2005), Rapid climate change in the ocean west of the Antarctic Peninsula during the second half of the 20th century, *Geophys. Res. Lett.*, *32*, L19604, doi:10.1029/2005GL024042.
Morris, E. M., and D. G. Vaughan (2003), Spatial and temporal variation of surface temperature on the antarctic peninsula and the limit of viability of ice shelves, in *Antarctic Peninsula Climate Variability: Historical and Paleoenvironmental Perspectives*, edited by E. Domack et al., pp. 61–68, AGU, Washington, D. C., doi:10.1029/AR079p0061.
Pattyn, F., et al. (2013), Grounding-line migration in plan-view marine ice-sheet models: Results of the ice2sea MISMIP3d intercomparison, *J. Glaciol.*, *59*(215), 410–422, doi:10.3189/2013JoG12J129.
Pollard, D., and R. M. DeConto (2012), Description of a hybrid ice sheet-shelf model, and application to Antarctica, *Geosci. Model Dev.*, *5*(5), 1273–1295, doi:10.5194/gmd-5-1273-2012.
Pritchard, H. D., R. J. Arthern, D. G. Vaughan, and L. A. Edwards (2009), Extensive dynamic thinning on the margins of the Greenland and Antarctic ice sheets, *Nature*, *461*(7266), 971–975, doi:10.1038/nature08471.
Pritchard, H. D., S. R. M. Ligtenberg, H. A. Fricker, D. G. Vaughan, M. R. van den Broeke, and L. Padman (2012), Antarctic ice-sheet loss driven by basal melting of ice shelves, *Nature*, *484*(7395), 502–505, doi:10.1038/nature10968.

Radic, V., and R. Hock (2011), Regionally differentiated contribution of mountain glaciers and ice caps to future sea-level rise, *Nat. Geosci.*, *4*(2), 91–94, doi:10.1038/ngeo1052.
Radic, V., A. Bliss, A. C. Beedlow, R. Hock, E. Miles, and J. G. Cogley (2014), Regional and global projections of twenty-first century glacier mass changes in response to climate scenarios from global climate models, *Clim. Dyn.*, *42*(1–2), 37–58, doi:10.1007/s00382-013-1719-7.
Riedl, C., H. Rott, and W. Rack (2004), Recent variations of Larsen Ice Shelf, Antarctic Peninsula, observed by Envisat, *paper presented at the ERS-ENVISAT Symposium*, ESA Spec. Publ., Salzburg, Austria, 6–10 September, (ESA SP-572, April 2005).
Rignot, E., and S. S. Jacobs (2002), Rapid bottom melting widespread near Antarctic ice sheet grounding lines, *Science*, *296*(5575), 2020–2023, doi:10.1126/science.1070942.
Rignot, E., G. Casassa, P. Gogineni, W. Krabill, A. Rivera, and R. Thomas (2004), Accelerated ice discharge from the Antarctic Peninsula following the collapse of Larsen B ice shelf, *Geophys. Res. Lett.*, *31*, L18401, doi:10.1029/2004GL020697.
Rignot, E., G. Casassa, S. Gogineni, P. Kanagaratnam, W. Krabill, H. Pritchard, A. Rivera, R. Thomas, J. Turner, and D. Vaughan (2005), Recent ice loss from the Fleming and other glaciers, Wordie Bay, West Antarctic Peninsula, *Geophys. Res. Lett.*, *32*, L07502, doi:10.1029/2004GL021947.
Rignot, E., J. Mouginot, and B. Scheuchl (2011), Antarctic grounding line mapping from differential satellite radar interferometry, *Geophys. Res. Lett.*, *38*, L10504, doi:10.1029/2011GL047109.
Rignot, E., S. Jacobs, J. Mouginot, and B. Scheuchl (2013), Ice-shelf melting around Antarctica, *Science*, *341*(6143), 266–270, doi:10.1126/science.1235798.
Rott, H., P. Skvarca, and T. Nagler (1996), Rapid collapse of northern Larsen Ice Shelf, Antarctica, *Science*, *271*(5250), 788–792, doi:10.1126/science.271.5250.788.
Rott, H., W. Rack, P. Skvarca, and H. De Angelis (2002), Northern Larsen ice shelf, Antarctica: Further retreat after collapse, *Ann. Glaciol.*, *34*(1), 277–282, doi:10.3189/172756402781817716.
Rott, H., W. Rack, and T. Nagler (2007), Increased export of grounded ice after the collapse of northern Larsen Ice Shelf, Antarctic Peninsula, observed by Envisat ASAR, in *International in Geoscience and Remote Sensing Symposium (IGARSS)*, pp. 1174–1176, IEEE, Barcelona, doi:10.1109/IGARSS.2007.4423013.
Rott, H., F. Müller, T. Nagler, and D. Floricioiu (2011), The imbalance of glaciers after disintegration of Larsen-B ice shelf, Antarctic Peninsula, *Cryosphere*, *5*(1), 125–134, doi:10.5194/tc-5-125-2011.
Rott, H., D. Floricioiu, J. Wuite, S. Scheiblauer, T. Nagler, and M. Kern (2014), Mass changes of outlet glaciers along the Nordensjköld Coast, northern Antarctic Peninsula, based on TanDEM-X satellite measurements, *Geophys. Res. Lett.*, *41*, 8123–8129, doi:10.1002/2014GL061613.
Sasgen, I., H. Konrad, E. R. Ivins, M. R. Van den Broeke, J. L. Bamber, Z. Martinec, and V. Klemann (2013), Antarctic ice-mass balance 2003 to 2012: Regional reanalysis of GRACE satellite gravimetry measurements with improved estimate of glacial-isostatic adjustment based on GPS uplift rates, *Cryosphere*, *7*(5), 1499–1512, doi:10.5194/tc-7-1499-2013.
Scambos, T. A., C. Hulbe, M. Fahnestock, and J. Bohlander (2000), The link between climate warming and break-up of ice shelves in the Antarctic Peninsula, *J. Glaciol.*, *46*(154), 516–530, doi:10.3189/172756500781833043.
Scambos, T. A., J. A. Bohlander, C. A. Shuman, and P. Skvarca (2004), Glacier acceleration and thinning after ice shelf collapse in the Larsen B embayment, Antarctica, *Geophys. Res. Lett.*, *31*, L18401, doi:10.1029/2004GL020670.
Scambos, T. A., T. M. Haran, M. A. Fahnestock, T. H. Painter, and J. Bohlander (2007), Modis-based Mosaic of Antarctica (MOA) data sets: Continent-wide surface morphology and snow grain size, *Remote Sens. Environ.*, *111*(2–3), 242–257, doi:10.1016/j.rse.2006.12.020.
Scambos, T. A., E. Berthier, and C. A. Shuman (2011), The triggering of subglacial lake drainage during rapid glacier drawdown: Crane Glacier, Antarctic Peninsula, *Ann. Glaciol.*, *52*(59), 74–82, doi:10.3189/172756411799096204.
Scambos, T. A., E. Berthier, T. Haran, C. A. Shuman, A. J. Cook, S. R. M. Ligtenberg, and J. Bohlander (2014), Detailed ice loss pattern in the northern Antarctic Peninsula: Widespread decline driven by ice front retreats, *Cryosphere*, *8*(6), 2135–2145, doi:10.5194/tc-8-2135-2014.
Schoof, C. (2007), Ice sheet grounding line dynamics: Steady states, stability, and hysteresis, *J. Geophys. Res.*, *112*, F03S28, doi:10.1029/2006JF000664.
Shepherd, A., D. Wingham, T. Payne, and P. Skvarca (2003), Larsen Ice Shelf has progressively thinned, *Science*, *302*(5646), 856–859, doi:10.1126/science.1089768.
Shepherd, A., D. Wingham, D. Wallis, K. Giles, S. Laxon, and A. V. Sundal (2010), Recent loss of floating ice and the consequent sea level contribution, *Geophys. Res. Lett.*, *37*, L13503, doi:10.1029/2010GL042496.
Shepherd, A., et al. (2012), A reconciled estimate of ice-sheet mass balance, *Science*, *338*(6111), 1183–1189, doi:10.1126/science.1228102.
Taylor, K. E., R. J. Stouffer, and G. A. Meehl (2011), An overview of CMIP5 and the experiment design, *Bull. Am. Meteorol. Soc.*, *93*(4), 485–498, doi:10.1175/BAMS-D-11-00094.1.
Turner, J., et al. (2013), Antarctic climate change and the environment: An update, *Polar Record*, *50*(03), 237–259, doi:10.1017/S0032247413000296.
van den Broeke, M. (2005), Strong surface melting preceded collapse of Antarctic Peninsula ice shelf, *Geophys. Res. Lett.*, *32*, L12815, doi:10.1029/2005GL023247.
Vaughan, D., G. Marshall, W. Connolley, C. Parkinson, R. Mulvaney, D. Hodgson, J. King, C. Pudsey, and J. Turner (2003), Recent rapid regional climate warming on the Antarctic Peninsula, *Clim. Change*, *60*(3), 243–274, doi:10.1023/A:1026021217991.
Vaughan, D. G. (2006), Recent trends in melting conditions on the Antarctic Peninsula and their implications for ice-sheet mass balance and sea level, *Arctic, Antarct. Alpine Res.*, *38*(1), 147–152, doi:10.1657/1523-0430(2006)038[0147:RTIMCO]2.0.CO;2.
Vaughan, D. G., and R. Arthern (2007), Why is it hard to predict the future of ice sheets?, *Science*, *315*(5818), 1503–1504, doi:10.1126/science.1141111.
Vaughan, D. G., and C. S. M. Doake (1996), Recent atmospheric warming and retreat of ice shelves on the Antarctic Peninsula, *Nature*, *379*(6563), 328–331, doi:10.1038/379328a0.
Vieli, A., and A. J. Payne (2005), Assessing the ability of numerical ice sheet models to simulate grounding line migration, *J. Geophys. Res.*, *110*, F01003, doi:10.1029/2004JF000202.
Williams, C. R., R. C. Hindmarsh, and R. J. Arthern (2012), Frequency response of ice streams, *Proc. R. Soc. A*, *468*, 3285–3310, Royal Society.
Winkelmann, R., M. A. Martin, M. Haseloff, T. Albrecht, E. Bueler, C. Khroulev, and A. Levermann (2011), The Potsdam Parallel Ice Sheet Model (PISM-PIK)—Part 1: Model description, *Cryosphere*, *5*(3), 715–726, doi:10.5194/tc-5-715-2011.
Wouters, B., A. Martin-Español, V. Helm, T. Flament, J. M. van Wessem, S. R. M. Ligtenberg, M. R. van den Broeke, and J. L. Bamber (2015), Dynamic thinning of glaciers on the southern Antarctic Peninsula, *Science*, *348*(6237), 899–903, doi:10.1126/science.aaa5727.
Wuite, J., H. Rott, M. Hetzenecker, D. Floricioiu, J. De Rydt, G. H. Gudmundsson, T. Nagler, and M. Kern (2015), Evolution of surface velocities and ice discharge of Larsen B outlet glaciers from 1995 to 2013, *Cryosphere*, *9*(3), 957–969, doi:10.5194/tc-9-957-2015.